Journal of Environmental Management 263 (2020) 110411

Contents lists available at ScienceDirect

Journal of Environmental Management

journal homepage: http://www.elsevier.com/locate/jenvman

Research article

Hot corrosion behaviors of TP347H and HR3C stainless steel with KCl deposit in oxy-biomass combustion

Jiaye Zhang [a], Zia ur Rahman [a], Xuebin Wang [a,*], Zhao Wang [a,b], Peng Li [c], Yongbing Wang [c], Delige Bate [c], Ke Zhao [d], Houzhang Tan [a]

[a] MOE Key Laboratory of Thermo-Fluid Science and Engineering, Xi'an Jiaotong University, Xi'an, 710049, China
[b] Xi'an Thermal Power Research Institute Co., Ltd., Xi'an, 710054, China
[c] Xinjiang Uygur Autonomous Region Special Equipment Inspection and Research Institute, Urumqi, 830000, China
[d] School of Environmental and Municipal Engineering, Xi'an University of Architecture and Technology, Xi'an, 710048, China

ARTICLE INFO

Keywords:
Biomass
Oxy-combustion
Hot corrosion
KCl deposit

ABSTRACT

Oxy-combustion is one of the most promising technologies for carbon capture and sequestration. When CO_2-neutral biomass is burned under oxy-combustion conditions, named "oxy-biomass combustion" a negative CO_2 emission can be achieved. However, the high content of potassium and chlorine in biomass results in sever ash deposition and corrosion in air fired furnaces, which are further aggravated in oxy-combustion mode due to the enrichment of corrosive species by flue gas recycle. In this paper, the hot corrosion behaviors and mechanism of two representative materials (TP347H, HR3C) used for superheaters in furnaces are studied. The effects of oxy-combustion atmosphere, KCl deposition, effect of SO_2, effect of water vapor, and temperature on the corrosion kinetics at the starting stage are investigated. The corrosion severity of the materials was determined using the weight gain method, and the microstructures and chemical compositions of corrosion layers were characterized by the scanning electron microscopy with energy dispersive spectroscopy, and X-ray diffraction. The results show that the hot corrosion rate is significantly sped up by KCl deposition, more than five times the gas corrosion rate under the same gas composition and temperature. HR3C with higher Cr and Ni contents is more likely to form Cr enrichment on the interface between the corrosion layer and the substrate than TP347H, resulting in stronger resistance to the hot corrosion than TP347H. When the corrosion atmosphere is changed from air-combustion to oxy-combustion, the hot corrosion rate is reduced with a denser Cr oxide film and less metal sulfides. The increase of temperature in the presence of KCl deposition significantly affects the hot corrosion rate, e.g. the corrosion rate at 650 °C is 16 times higher than that at 450 °C. Water vapor and SO_2 concentrations have opposite influences on the hot corrosion, respectively. Compared to the dry environment, a high-humidity environment decreases the hot corrosion rate; however, a higher SO_2 concentration facilitates the sulfation of KCl deposits, leading to stronger damage to the chromium oxide film and thereby an increased hot corrosion rate.

1. Introduction

Biomass has a vital role to play in promoting renewable energy and in reducing the potential environmental impact of fossil fuel combustion (Smith et al., 2019). Oxy-biomass combustion coupled with carbon capture and sequestration (CCS) processes can lead to 'carbon negative' technology, i.e. not only avoiding additional CO_2 emissions but also helping to reduce atmospheric CO_2 emissions (Sher et al., 2018). However, compared to coal, the significant characteristics of biomass is of high contents of potassium and chlorine. Potassium and chlorine in biomass aggravate the ash deposition, fouling, slagging, and corrosion in furnaces burning biomass (Blomberg et al., 2019).

The degree of fouling and corrosion depends on the existing form and evolution of potassium and chlorine during biomass combustion (Cao et al., 2016). Potassium is found associated with the fuel moisture as water-soluble salts or reacted with the organic functional groups (carboxylic, phenolic) of the lignocellulose matrix (Chen et al., 2017). During the thermochemical conversion of biomass, the potassium in biomass is released into flue gas at high temperatures. These potassium species can further react or undergo physical transformations to

* Corresponding author.
E-mail address: wxb005@mail.xjtu.edu.cn (X. Wang).

https://doi.org/10.1016/j.jenvman.2020.110411
Received 12 December 2019; Received in revised form 22 February 2020; Accepted 6 March 2020
Available online 11 March 2020
0301-4797/

condense and form aerosols, which can deposit on the heat exchanger surfaces. These deposits can react with the metals of the heat exchanger, resulting in severer hot corrosions (Cao et al., 2016). Pettersson et al. (2011) studied the effect of the chlorides, sulfates, and carbonates of potassium on hot corrosion of 304 stainless steel and concluded that K_2CO_3 and KCl are equally corrosive toward 304 stainless steel while K_2SO_4 is much less corrosive. K_2CO_3 and KCl can react with the chromium-rich oxide on metal surfaces, forming K_2CrO_4. The resulted chromium depletion of the protective oxide layer causes rapid corrosion in the O_2–H_2O atmosphere. Blomberg et al. (2019) studied the chemical reactions involved with furnace exposure of KCl and KOH with Cr_2O_3 and concluded that the reaction of KCl with Cr_2O_3 involves an intermediate KOH generated before K_2CrO_4 is formed. Mahajan and Chhibber (2019) investigated the corrosion behavior of different power plant steels exposed to the different salt mixture at 950 °C and concluded that steel containing higher Cr content possesses better corrosion resistance to the molten salt mixture exposure. The presence of KCl in combination with Na_2SO_4 is the main corrosion enhancement factor in hot corrosion behavior. Meißner et al. (2019) analyzed the effect of three coatings (Cr, Ni + Cr, Ni–P + Cr) on ferritic-martensitic X20CrMoV12-1 steel in a biomass-co-firing atmosphere and summarized that beneath the deposit of Na_2SO_4–K_2SO_4 the coatings proved to be highly resistant whereas addition of KCl drastically accelerated the corrosive attack.

Under oxy-combustion conditions, the flue gas recycle enriches the concentration of corrosive gas species in furnaces, e.g. the concentrations of sulfur oxide and hydrogen chlorine increase by 3–4 times compared with that in conventional air-combustion. Bordenet (2008) found that the flue gas composition was changed when the atmosphere was converted from conventional air-combustion to oxy-combustion, which also changed the chemical composition of the deposited layer. As a result, the corrosion was aggravated under oxy-combustion conditions. Paneru et al. (2013) studied the molten salt corrosion behaviors of Alloy310 and Alloy 314 in oxy-combustion and found that the corrosion rate in air combustion mode is faster. Holcomb et al. (2012) found that the corrosion rate of TP347H in air combustion mode was faster than that in oxy-combustion mode, while T91 showed the opposite trend.

In summary, the high-temperature corrosion by gas and molten potassium salts from biomass combustion has been widely studied under conventional air-combustion conditions. However, only a few studies have been conducted on high-temperature corrosions under oxy-combustion conditions, especially for molten potassium-salt corrosion (hot corrosion). Depending on the complex gas compositions and metal materials, the conclusions on the effect of atmosphere change from air-combustion to oxy-combustion on hot corrosion of potassium salt are still not consistent, and the hot corrosion mechanism under oxy-combustion conditions is not well understood.

This paper aims to demonstrate the hot corrosion mechanism and kinetics in biomass combustion when the atmosphere is changed from air-combustion to oxy-combustion. The hot corrosion behaviors of two representative materials (TP347H, HR3C) used for superheaters in furnaces are studied. The effects of oxy-combustion atmosphere, KCl deposition, effect of SO_2, effect of water vapor, and temperature on the corrosion kinetics at the starting stage are investigated. The corrosion severity of the materials was determined using the weight gain method, and the microstructures and chemical compositions of corrosion layers were characterized by the scanning electron microscopy with energy dispersive spectroscopy (SEM-EDS) and X-ray diffraction (XRF).

2. Materials and methods

2.1. Materials

Two alloy materials, HR3C and TP347H were used in the test, which have been most commonly used in the superheater and reheater tubes in utility boilers. The compositions of the two samples are shown in Table 1. The samples with the dimension of 10 mm × 10 mm × 3 mm were cut from the actual superheater tubes by using a wire-cutter. After burnishing the surface of samples, the samples were cleaned for 1 h in acetone solution using an ultrasonic cleaning device. The sample was used in the test after being dried in the oven.

2.2. Depositing method of KCl vapor on steel surfaces

Many methods have been used to deposit the salt layer on the heating surface. McKee et al. (1978) immersed the alloy coupons in a crucible containing melting salt, and a thermo-balance system, i.e. temperature and pressure, was used to preserve the desired environment. Lin et al. (2007) just brushed the salt solution to make the salt film. Yu et al. (2019) immersed the alloy specimens in a concentrated salt solution and dried them at 100 °C to form a salt film. Mahobia et al. (2013) used the spray technique for salt coating on the sample surface. While in the actual combustion process, the salts present in the combusting fuel vaporized in a high-temperature area and then condensed on low-temperature surfaces (Hu et al., 2018). However, no method was able to achieve a real and uniform deposition of KCl vapor similar to the practical situation in industries. Therefore, in this study, we adopt a new KCl deposition approach that is more specific and very similar to the practical situation of the industry. The schematic of the depositing system is shown in Fig. 1. First, the temperature of the corundum boat containing KCl was increased up to 800 °C, at which the KCl evaporated and then carried by N_2 to the cooled area at 300 °C (monitored by a K-type thermocouple), where it condensed on the surface of the metal sample fixed in the specimen deposition fixture. The sample metal surface before and after depositing with KCl is shown in Fig. 1(a) and (b). The micromorphology of the sample surface after KCl depositing was uniform and similar to the industries practical depositions.

2.3. Method of corrosion test

The schematic of the corrosion test system is shown in Fig. 2, consisting of gas feeding, heating furnace, and exhaust gas collecting part respectively. The corundum boat containing alloy samples was placed into the isothermal zone of the quartz tube with a diameter of 40 mm and a length of 1000 mm. The steam generated by the heater was carried by the balance gas and mixed with O_2 and SO_2 at the inlet of the reactor, and maintain a total flow rate of 500 ml min^{-1}. The temperature of the inner reaction zone was detected by using a K-type thermocouple.

To investigate the mechanism of the hot corrosion at the early stage, we exposed the alloy samples in a simulated flue gas environment (SO_2–O_2–H_2O–CO_2/N_2) for 8 h and measured the mass gain per 2 h. Although the fuel-sulfur conversion ratio is not changed significantly in oxy-combustion, but due to the recycled flue gas, the SO_2 concentration increases significantly than air-fuel combustion (Chen et al., 2012). In this study, the concentration of SO_2 is determined as 0.2 vol % in the simulated oxy-combustion environment. The detailed experimental conditions are provided in Table 2.

A weight gain (mg/cm^2) versus time plot was employed to investigate the kinetic analysis of hot corrosion, for 4 cycles. After each cycle, samples were weighted by using a microbalance with a sensitivity of ±0.001 mg. The mass gain and average corrosion rate can be obtained by:

$$y = (W_2 - W_1)/\mathrm{A} \quad (1)$$

$$V = y/t \quad (2)$$

where: y – mass gain per hectare (mg·cm^{-2}); W_2 – mass of sample after corrosion (mg); W_1 – mass of sample before corrosion (mg); A – sample surface area (cm^2); t – corrosion time (h); V – average corrosion rate (mg·cm^{-2}·h^{-1}).

Table 1
Elemental compositions of TP347H and HR3C stainless steel samples.

Material	C	Mn	Si	Cr	S	Ni	P	Nb	N
TP347H	0.04–0.10	≤2.0	≤0.75	17–20	≤0.03	9–11	≤0.04	0.6–0.8	/
HR3C	0.04–0.10	≤2.0	≤0.75	24–26	≤0.03	17–23	≤0.03	0.02–0.60	0.15–0.35

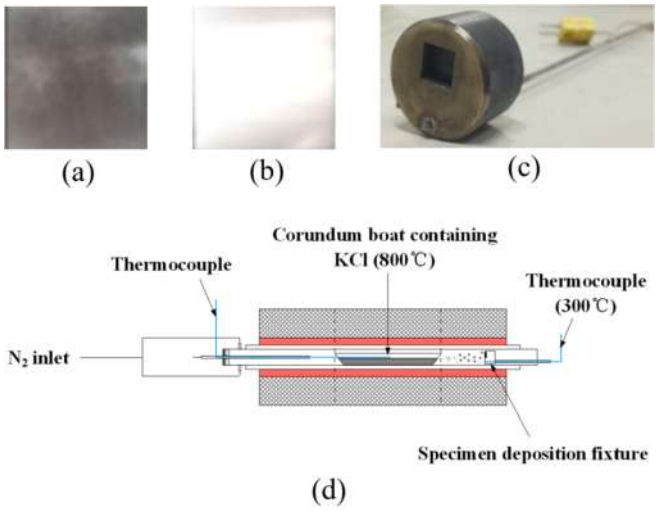

Fig. 1. Schematic of KCl vapor deposition on steel sample surfaces (a, before depositing; b, after depositing; c, fixture; d, system of salt vapor deposition on steel sample surface).

2.4. Methods of sample characterization and corrosion kinetics analysis

Several expressions, like linear, parabolic and logarithmic law have been used to fit the corrosion mass gain as a function of exposure time (Little, 2008; Mahobia et al., 2013). In this study, the parabolic law is adopted stated by Equation (3),

$$y = k \cdot t^2 \tag{3}$$

where k represents the oxidation rate constant regarding the ability of corrosion resistance of the alloy material. K depends upon the property of alloy material, reaction temperature, and reaction atmosphere. In this work, the weight gain plots agree very well the parabolic rate law.

After obtaining the weight gain information, the Scanning Electron Microscope (SEM, JOEL JSM-6390 A) and X-ray Diffraction (XRD, X'Pert Pro) were used to examine the microstructure and chemical composition of the sample surface after corrosion. The samples were mounted by liquid epoxy resin to get the micro information of cross-section. The oxidation layer was scratched and milled to prepare for XRD analysis.

3. Results and discussion

3.1. Performance of KCl vapor deposition on sample surfaces

First, the salt deposition rate is calibrated as shown in Fig. 3. In the time range of 0–0.5 h, the amount of salt deposition increases rapidly and also the deposition rate is higher as compared to the rate after 0.5 h. After 0.5 h, the deposition rate becomes constant and the salt weight gain increases linearly. Since the salt depositing process is related to the difference between the temperature of the fixture and the temperature of the incoming gas stream. At the start, the temperature of the fixture is comparatively lower in the quartz tube, resulting in a large temperature difference and thereby a high deposition rate. Following certain KCl deposition, the fixture gradually heats up, resulting in a reduction in the deposition rate to a constant level.

Table 2
Experiment conditions for hot corrosion tests.

	Temperature/°C	Gas composition/vol. %				KCl deposition /mg.cm^{-2}
		SO_2	O_2	H_2O	Balance	
TP347H	550	0.2	2	20	CO_2	0
	550	0.2	2	0	N_2	0.5
	550	0.3	2	20	N_2	0.5
	450	0.2	2	20	CO_2	0.5
	550	0.2	2	20	CO_2	0.5
	650	0.2	2	20	CO_2	0.5
	550	0.2	2	0	CO_2	0.5
	550	0.2	2	20	CO_2	1.0
	550	0.3	2	20	CO_2	0.5
HR3C	550	0.2	2	20	CO_2	0
	550	0.2	2	0	N_2	0.5
	450	0.2	2	20	CO_2	0.5
	550	0.2	2	20	CO_2	0.5
	650	0.2	2	20	CO_2	0.5
	550	0.2	2	0	CO_2	0.5
	550	0.2	2	20	CO_2	1.0
	550	0.3	2	20	CO_2	0.5

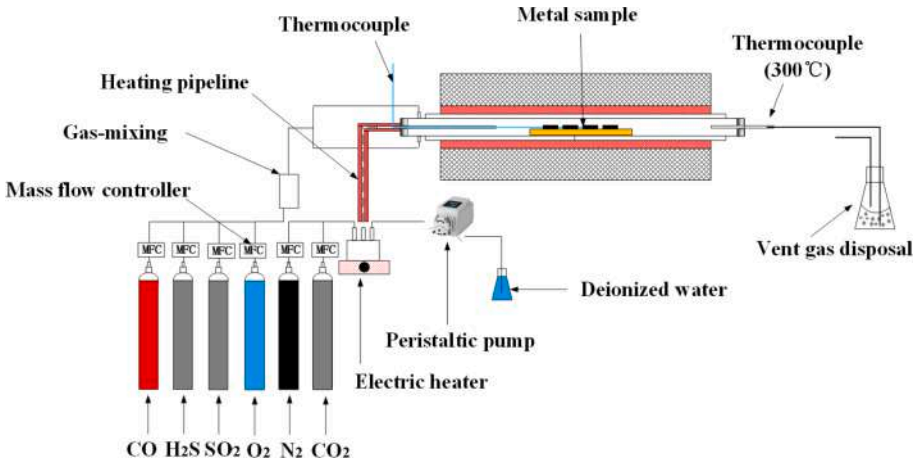

Fig. 2. Schematic of high-temperature corrosion experimental system.

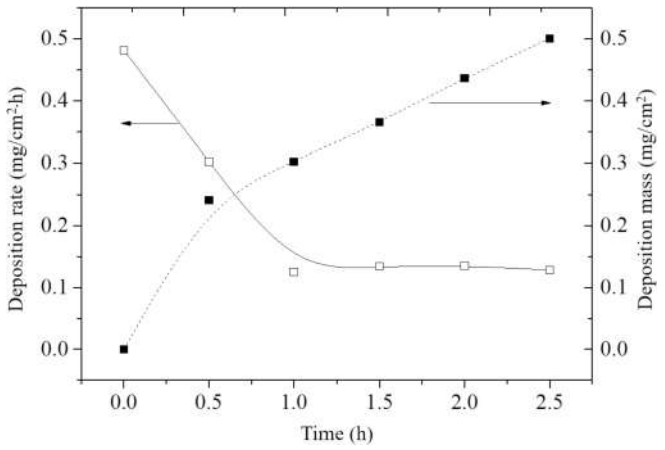

Fig. 3. Deposition behavior of KCl by time.

The micromorphology of the specimen surface after salt plating is shown in Fig. 4; it can be noticed that a uniform and continuous salt film is formed on the surface of the test component. A relatively loose salt layer is observed on the surface as compared with the untreated test piece. Further, there is no obvious corrosion problem, which shows that the salt plating used in this experiment is feasible and will not seriously interfere with the subsequent high-temperature corrosion experiment.

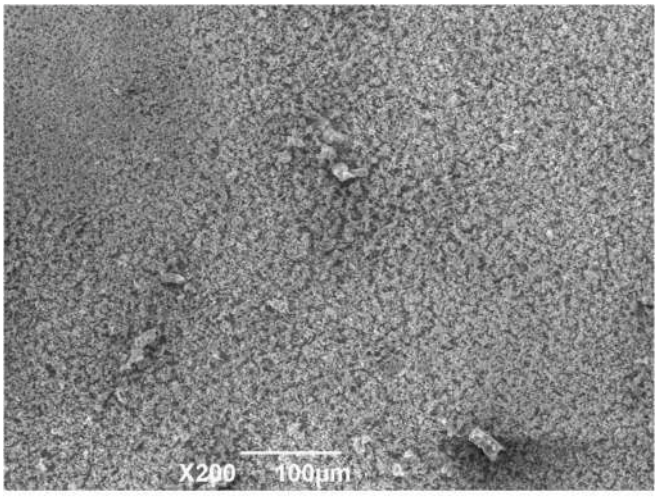

Fig. 4. Micromorphology of sample surface after being coated (a, 200 times; b, 2000 times).

3.2. Corrosion kinetics at various environments

3.2.1. Comparison of corrosion behaviors in pure gas phase and with KCl deposits

Two samples of alloys, TP347H and HR3C were used to assess the corrosion impact of KCl deposits. As shown in Fig. 5, the weight gain curves of corrosion is an agreement with the parabolic law. In addition, without KCl deposition, the rate constant a and average corrosion rate V of TP347H were 0.040 and 0.0135 mg $cm^{-2}{\cdot}h^{-1}$, whereas for HR3C were 0.035 and 0.0116 mg $cm^{-2}{\cdot}h^{-1}$ respectively. After the salt deposition, the corrosion rate of the two materials TP347H and HR3C increased sharply by 5.32 and 5.17 times respectively. Especially in the first 2 h, the weight gain rate increased about 8 times. It is evident that the deposition of salt on metal surfaces has a very drastic effect on the corrosion behavior compared to the gas corrosion rate under the same gas composition and temperature (Zeng et al., 2014). According to the reaction (4) and (5), KCl directly react with the oxide scale, which severely aggravate the alloy corrosion (Grabke et al., 1995).

$$Fe_2O_3 + 2KCl + 1/2O_2 = K_2Fe_2O_4 + Cl_2 \quad (4)$$

$$Cr_2O_3 + 4KCl + 5/2O_2 = 2K_2CrO_4 + 2Cl_2 \quad (5)$$

$$Fe + Cl_2 = FeCl_2 \quad (6)$$

Accompany with the erosion of the dense oxide scale, molecular chlorine liberated in reaction (4) and (5) respectively, react with iron and formed iron chloride at the interface of the substrate and corrosion scale by reaction (6) which make more adverse the corrosion effect (Grabke et al., 1995).

Meanwhile, the degree of sulphation of the injected KCl increases substantially in oxy-combustion compared to air combustion conditions (Ekvall et al., 2017), and the presence of high concentration water vapor especially in wet combustion, would dramatically enhance the destruction of protective oxide film (Ani et al., 2009), which can increase the carburization of CO_2 into the alloy. Furthermore, the C element migrates into the alloy to form Cr_xC_y, which speeds up the Cr element migration to the surface of the alloy to form Cr_2O_3. While the evaluation of corrosion behavior of KCl and oxy-combustion atmosphere still need more research.

3.2.2. Effect of N_2 or CO_2 atmosphere as a balance gas

Corrosion experiment was carried out under two equilibrium gases N_2 and CO_2 in air-combustion and oxy-combustion respectively, to compare the behavior of molten salt corrosion of two alloy samples. It can be noticed in Fig. 6, that the corrosion rate of both materials in air-

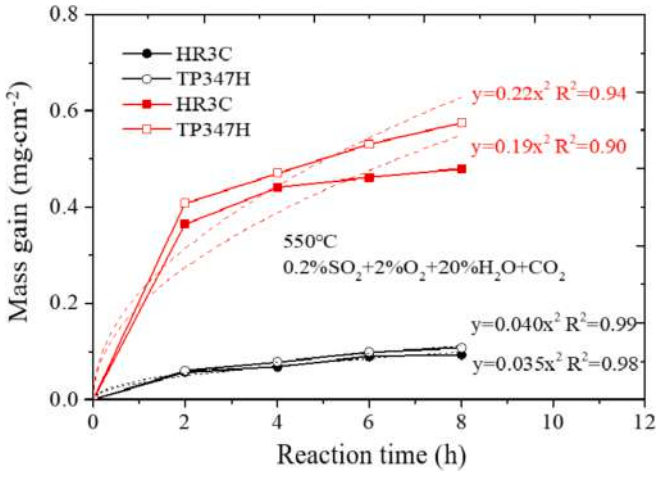

Fig. 5. Comparison of high-temperature (black) and hot corrosion (red). (2% O_2+0.2%SO_2+20%H_2O + CO_2, 550 °C) .

combustion is higher than oxy-combustions using CO_2 as balance gas. The parabolic rate constant "*k*" and the average corrosion rate for TP347H are 0.29 and 0.086 mg cm^{-2}. h^{-1}, respectively, in air combustion, which is 19.4% higher than that of oxy-combustion. Similarly, the "*k*" and corrosion rate for HR3C are 0.24 and 0.071 mg cm^{-2}. h^{-1} respectively, in air-combustion which is 18.3% larger than that of oxy-combustion.

There are different views about the hot corrosion in oxy-combustion. Bordenet (2008) noted that the chemistry of ash deposition is promptly changed in oxy-combustion as compared to air-combustion mode. This is due to the high concentration of CO_2 produced by the recycled flue gas, which promotes the formation of carbonates that impairs corrosion. Paneru et al. (2013) used the coal-fired fly ash to study the hot corrosion behavior of Alloy310 and 314 in the simulated flue gas. The rate of corrosion in air combustion mode was found to be higher. While the study of Holcomb et al. (2013) revealed that TP347H had a faster rate of corrosion in air-combustion than oxy-combustion, although T91 had no significant difference between air combustion and oxy-combustion environment. In short, the degree of corrosion closely related to alloy material type, deposited ash, and flue gas composition respectively. This paper found that a high concentration of CO_2 had a slight inhibitory effect on the process of molten salt corrosion of the two alloy materials (Ekvall et al., 2017). The Cr component of the alloy is expected to form a protective oxide layer under a high concentration of CO_2, leading to slightly less corrosion.

3.2.3. *Effect of temperature*

Three temperature points, 450 °C, 550 °C, and 650 °C were chosen to test the temperature effects on hot corrosion in oxy-combustion. As shown in Fig. 7, the increase in temperature has a significant effect on hot corrosion and the corrosion rate of both materials is increased drastically. At 650 °C, the average corrosion level is 16.45 times higher than that of 450 °C. Paul and Harvey (2013) performed different corrosion tests at high temperature environments for biomass applications and found that alloy-625, Alloy-718 and Alloy-726 coated with K_2SO_4– KCl layer showed a severe corrosion at high temperature ≥700 °C as compared to the corrosion gain at lower temperature ≤525 °C. Otsuka (2008) analyzed the flue gas vapor condensation of corrosive salts on heater tubes in incinerators and illustrated that when the temperature of flue gas become higher than the melting point of different salts like NaCl, KCl, and Na_2SO_4 it leads to a severe corrosion on the super heater tubes. This can be interpreted from the fact that high-temperature flue gases generally have high concentration of vapor NaCl and KCl, and hence have greater capability to vapor-condense these species on tube surfaces.

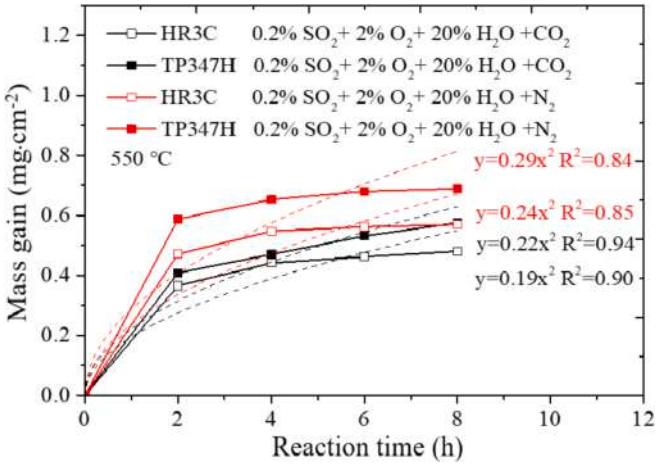

Fig. 6. Mass gain kinetic curves comparison in oxy-combustion and air atmosphere. ($2\%O_2+0.2\%SO_2+20\%H_2O + CO_2/N_2$, 550 °C) .

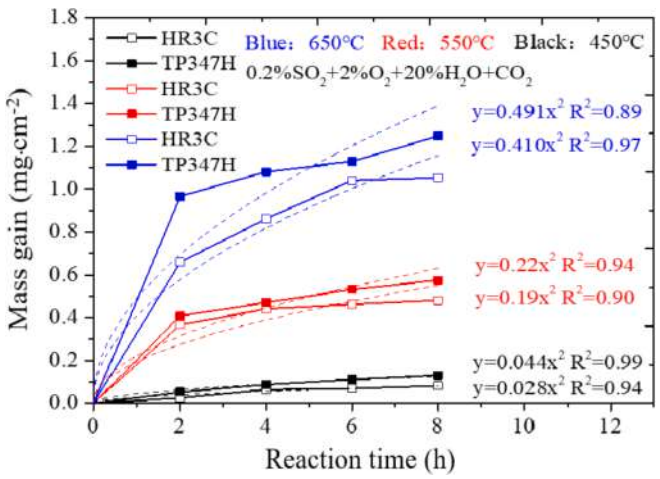

Fig. 7. Mass gain kinetic curves of two alloy materials in different temperature. ($2\%O_2+0.2\%SO_2+20\%H_2O + CO_2$, 450 °C, 550 °C, 650 °C) .

In short as the temperature rises, the diffusion and mass transfer of the reaction gas to the alloy material oxide layer becomes severe and the material corrosion resistance decreases linearly under high-temperature conditions, thus intensifying the corrosion process (Pettersson et al., 2011).

3.2.4. *Effect of wet or dry flue gas (moisture)*

To observe the effect of moisture on hot corrosion in oxy-combustion, two concentration levels of moisture were considered. It can be noticed from Fig. 8, that when the water vapor concentration increases from 0% to 20%, the average corrosion level of HR3C and TP347H is decreased by 93.1% and 71.7%, respectively. These results show a significant decrease in the corrosion rate for both materials in the moisture-rich condition.

The effect of H_2O vapor on the high temperature corrosion with the presence of alkali chloride has been discussed by many researchers (Asteman et al., 2002; Karlsson et al., 2014). Generally, H_2O have both the probability of inhabiting or promoting effect on corrosion process. Some experimental results revealed that the water vapor accelerate the sulfation process of alkali salts in hot corrosion in the presence of high SO_2 contents in the flue gas according to the reaction (7) and (8) respectively (Paneru et al., 2013).

$$2KCl + SO_2 + O_2 = K_2SO_4 + Cl_2 \quad (7)$$

$$2KCl + SO_2 + H_2O + 1/2O_2 = K_2SO_4 + 2HCl \quad (8)$$

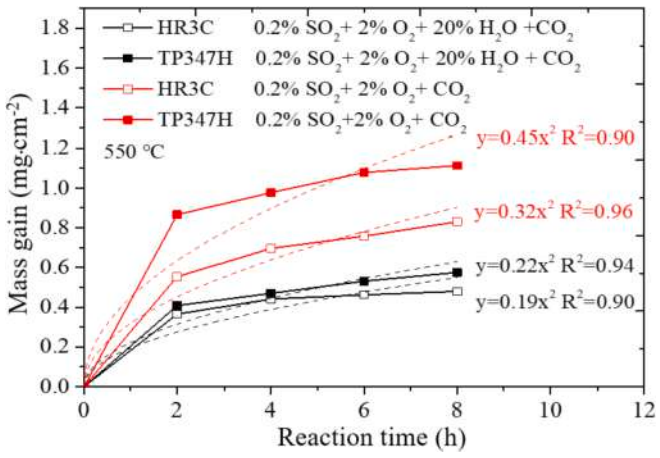

Fig. 8. Mass gain kinetics behavior in high moisture atmosphere $2\%O_2+0.2\%SO_2+0\%/20\%H_2O + CO_2$, 550 °C) .

The Cl_2 and HCl released during the reaction reacts with the substrate and oxide scale of the alloy, further exacerbating the corrosion. In the presence of water vapor, reaction (8) is more competitive than the reaction (7). Lehmusto et al. (2012) suggested that the reduction of alkali metal corrosion in a higher moisture concentration may due to the formation of denser and thus thinner oxide scale. Henriksson and Warnqvist. (1979) observed the inhibiting effect of water vapor to corrosion when it is present up to 10 vol % concentration. They explained that water concentration from 0 to 10% increase the sulfation reactions while above than 10% it show the opposite influence. Okoro et al. (2015) found the K_2SO_4 conversion fraction in the KCl was reduced significantly in the condition of 13 vol % H_2O compared with 3 vol % H_2O. They interpret that the water molecules compete the active sites existed in the deposit surface with SO_2, due to which the heterogeneous sulfation reaction become inferior. In our research work, the average concentration of water vapor is up to 20 vol %, which has suppressed the sulfation reaction resulting in the reduction of both alloys corrosion.

3.2.5. *Effect of SO_2 concentration*

To observe the effect of SO_2 on hot corrosion in oxy-combustion, two concentration levels of SO_2 for both alloy samples were considered. As shown in Fig. 9, an increase in SO_2 concentration can significantly increase the corrosion rate of both alloys. For the HR3C, the resistant ability to the SO_2 corrosion is better than the TP347H. The average corrosion rate for TP347H is increased by 32.7%.

When the concentration of SO_2 is high, the deposition of salt chloride on the alloy surface undergoes a sulfation process, as shown in reaction (7) and (8), accompany with the oxide film depletion (Grabke et al., 1995),

$$Cr_2O_3 + 3SO_3 = 2Cr^{3+} + 3SO_4^{2-} \quad (9)$$

Which destroys the alloy oxide film and sped up the reaction of composite sulfate which further degrade the alloy matrix, ultimately enhanced the corrosion (Okoro et al., 2017). Therefore, the increase in the concentration of SO_2 in the experiment promote the degradation of protective chromium oxide film, which makes the molten salt corrosion more serious.

3.3. *Discussion based on micro-morphologies and chemical-identification of corrosion products*

3.3.1. *2%O_2+0.2%SO_2+20%H_2O + CO_2 , 550 °C*

It can be seen from Fig. 10(a), that the relatively high Cr element is found in the HR3C corrosion layer, and the peak of the Cr element is located inside the corrosion layer, indicating that there is a clear diffusion of the Cr element from the bulk to the surface. The XRD analysis of the HR3C corrosion layer as shown in Fig. 11 (a) indicates that the main components of the corrosion surface are Fe_2O_3 and $(Fe_{0.6}Cr_{0.4})_2O_3$. This depicts that the presence of KCl inhibits the Cr oxide formation on the surface of HR3C, causing S element to diffuse into the substrate through the corrosion layer which leads to the enhancement of corrosion behavior (Pettersson et al., 2008).

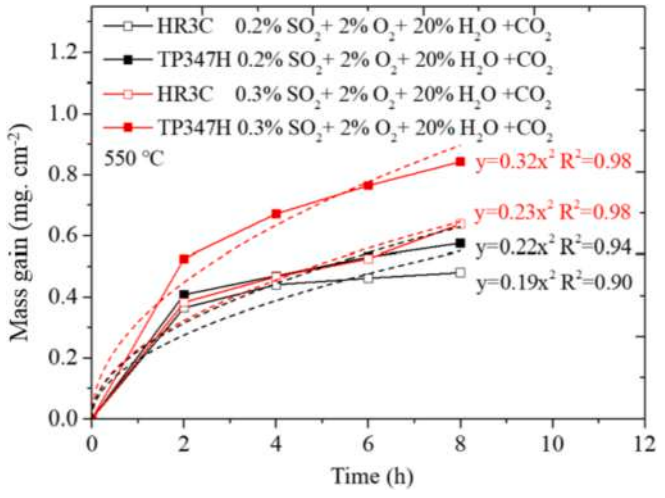

Fig. 9. Mass gain kinetics behavior in different SO_2 concentrations. (2% O_2+0.2/0.3%SO_2+20%H_2O + CO_2/N_2 , 550 °C) .

Compared with Fig. 10 (a), it can be seen from Fig. 10(b) that the corrosion layer of TP347H has a small content of Cr and mainly composed of Fe–O–S elements. The corrosion layer is tightly bonded to the matrix, and a weak Cr element enrichment phenomenon appears at the junction. Unlike HR3C, a phenomenon of infiltration into the grain limit, i.e. intergranular corrosion is present in the TP347H corrosion layer product. There is an increasing trend in the content of S from the junction to the grain boundary, suggesting a more severe corrosion behavior. The XRD analysis of the corrosion layer in combination with Fig. 11(b) shows that the corrosion layer products are mainly Fe_2O_3 and $(Fe_{0.6}Cr_{0.4})_2O_3$, and the sulfide Cr_5S_6 and carbide Fe_5C_2 are also observed, which further illustrates that the TP347H undergoes a more serious corrosion process.

The above results show that HR3C is more resistant to KCl molten salt corrosion and is mainly due to higher Cr content in HR3C (Mlonka-Mędrala et al., 2019). On the other hand, the surface of TP347H did not form a Cr oxide layer but instead formed a Cr sulfide that increases its corrosion.

3.3.2. *2%O_2+0.3%SO_2 +20%H_2O + N_2, 550 °C*

It can be seen from Fig. 12 (a) that the coexistence of K and S elements in the surface of sedimentary salt layer of HR3C, and it is evident that KCl has undergone a clear process of sulfation. The contents of Fe, O, and Cr in the outer edge of the corrosion layer are high, and there is an increasing trend of Ni element in the medium part of the corrosion surface. Meanwhile, the S element is high in the joint region with the matrix, and the S component penetrates deeply in the bulk of the substrate. From Fig. 12 (a), the XRD analysis of the HR3C corrosion layer shows that the main components are Fe_2O_3, $(Fe_{0.6}Cr_{0.4})_2O_3$ and $Fe_2Cr_2O_4$, and a small amount of $NiFe_2O_4$.

It can be seen from Fig. 12 (b) that severe spalling of oxide corrosion scale occurred. The oxide layer of TP347H is mainly composed of Fe and a small amount of Cr element and the enrichment of Cr element is not significant. There is more Cr in the joint between the corrosion layer and the matrix, but the contents of the O element are lower, indicating that the protective Cr–O layer is destroyed by sulfate. The intergranular corrosion occurs at the junction of the corrosion layer and the substrate, and the S element diffuses along the grain boundary to the inside of the bulk. The corrosion layer is relatively broken and has a loose structure. The XRD analysis of TP347H corrosion shown in Fig. 13 (b) shows that the main components are Fe_2O_3, K_2SO_4 and a small amount of Fe_9S_{10}, Fe_1-xS iron sulfide, which indicates the enhanced sulfation process and the erosion of S element to the bulk.

In summary, comparing the corresponding results of corrosion weight gain mentioned above, it can be noticed that, degree of corrosion of the two materials becomes more severe when N_2 is used as a balance gas (air-combustion) as compared to the oxy-combustion (Ekvall et al., 2017); also among the two samples alloy, the TP347H is more prone to sulfate corrosion than HR3C.

3.3.3. *2%O_2+0.2%SO_2 +CO_2, 550 °C*

It can be seen from Fig. 14 (a) that the corrosion layer of HR3C is mainly composed of Fe, Cr and O elements. High content of S, O was found in the sediment layer of the outermost surface, suggesting that there has been a clear sulfation phenomenon. The XRD analysis of the HR3C corrosion layer in Fig. 15 (a) shows that the main components are Fe_2O_3, Fe_3O_4 and $Fe_2Cr_2O_4$.

It can be observed in Fig. 14 (b) that the TP347H corrosion layer is

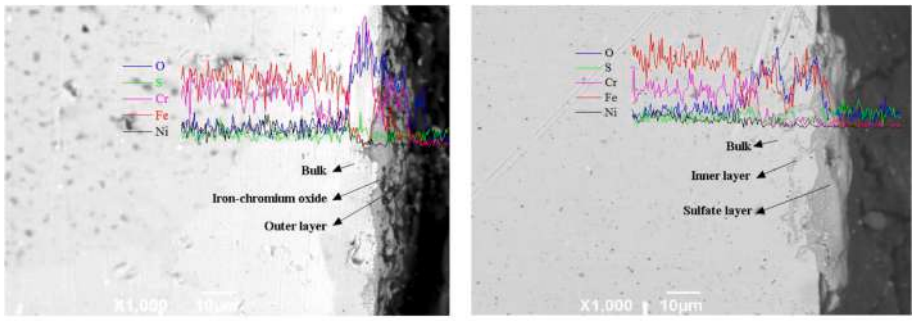

(a) HR3C, 550°C, 8h (b) TP347H, 550°C, 8h

Fig. 10. SEM and EDS line analysis of the sample cross-sections of HR3C and TP347H after 8 h corrosion test (2%O_2+0.2%SO_2+20%H_2O + CO_2).

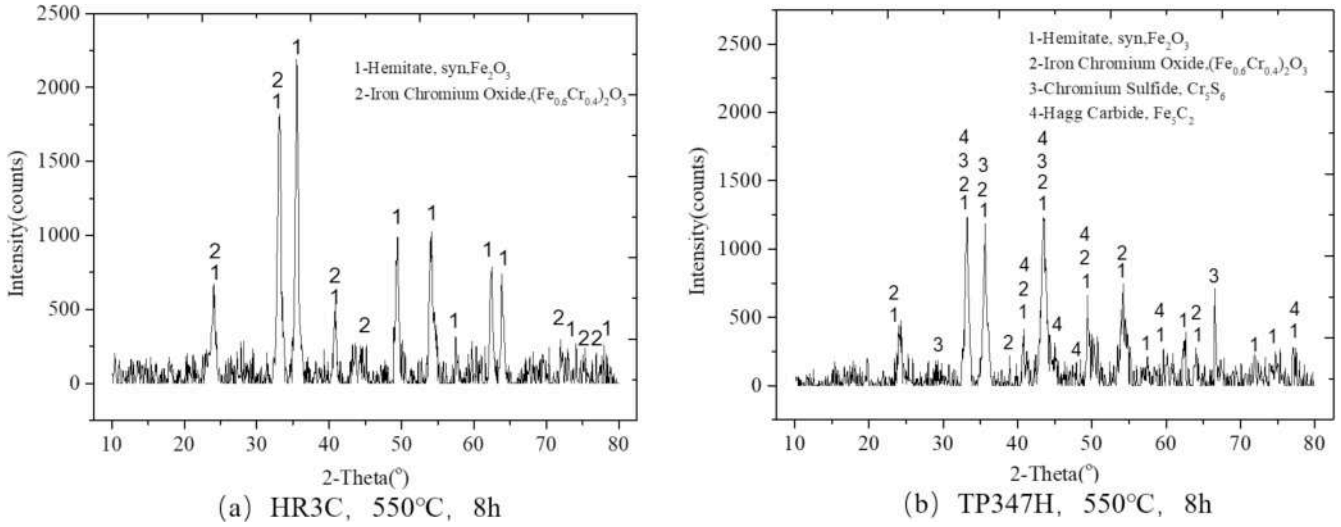

(a) HR3C, 550°C, 8h (b) TP347H, 550°C, 8h

Fig. 11. XRD patterns of the corrosion layer at 550 °C (2%O_2+0.2%SO_2+20%H_2O + CO_2) .

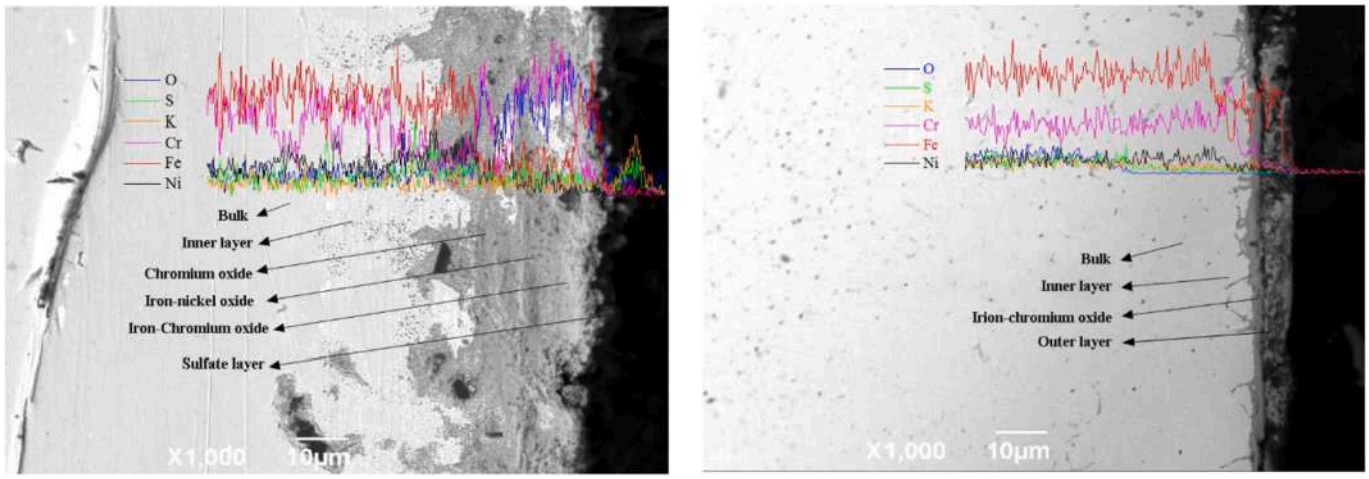

(a) HR3C, 550°C, 8h (b) TP347H, 550°C, 8h

Fig. 12. SEM and EDS line analysis of the sample cross-sections of HR3C and TP347H after 8 h.

mainly composed of Fe, Cr, and O elements. The structure of the corrosion layer is relatively loose, and there are many holes in the interior. Fig. 15 (b) shows that the main components are Fe_2O_3 and $Fe_2Cr_2O_4$ spinel, and a small amount of $NiFe_2O_4$.

In summary, corresponding with the weight gain results, it can be noticed that in a dry environment the corrosion layer penetrates deeply into the substrate and the corrosion structure is more broken and porous than that of the wet environment which validates the inhibiting behavior of moisture in hot corrosion (Okoro et al., 2015). In addition, compared with other conditions with 20% water vapor, both alkali metal sulphates and sulfide are not found in oxide scale of the two alloys in this case, which indicate that the water vapor may contribute to the

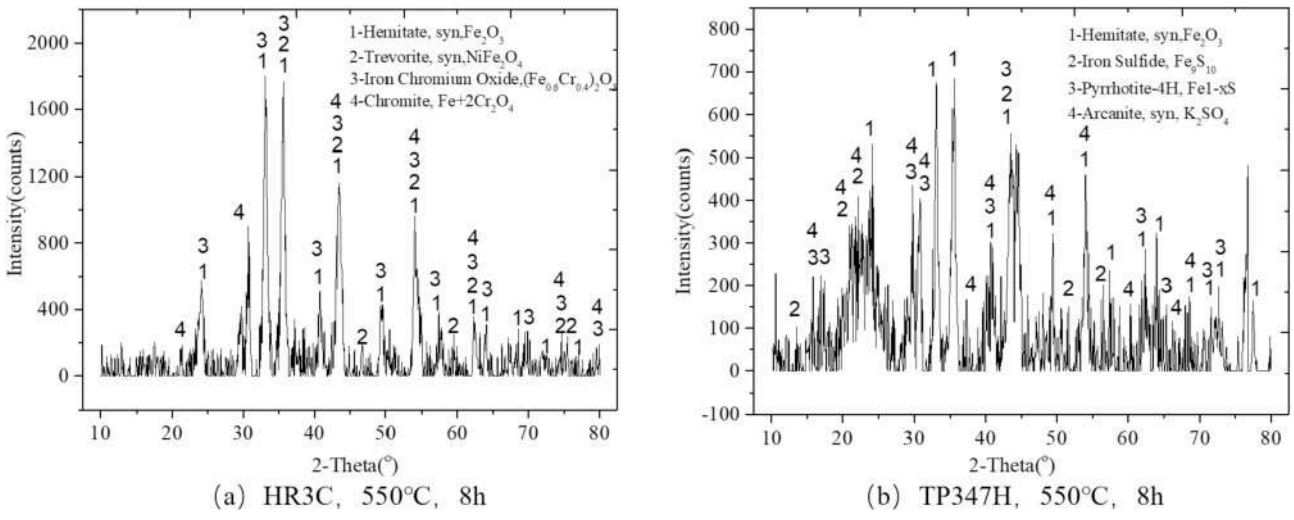

Fig. 13. XRD patterns of the corrosion layer at 550 °C ($2\%O_2+0.2\%SO_2+20\%H_2O + N_2$) .

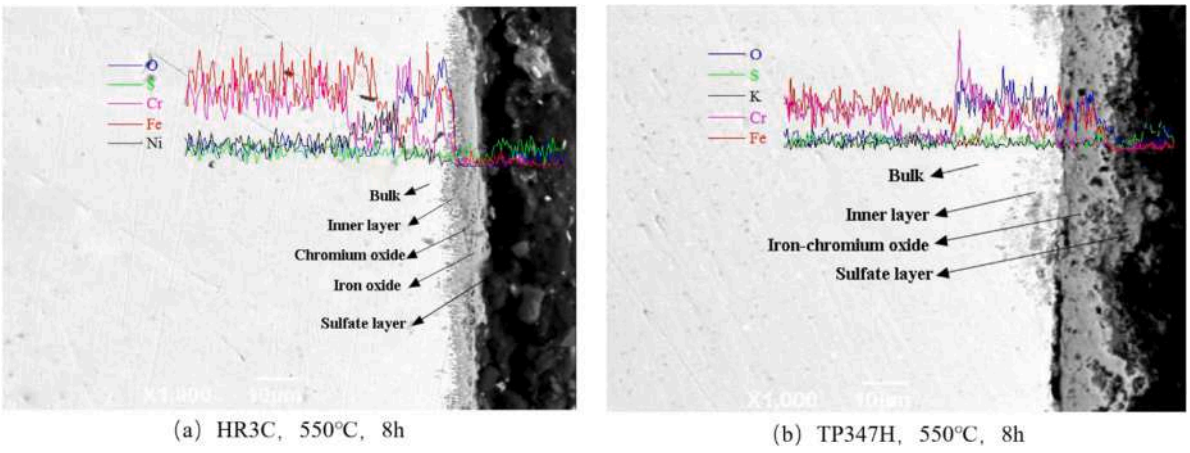

Fig. 14. SEM and EDS line analysis of the sample cross-sections of HR3C and TP347H after 8 h.

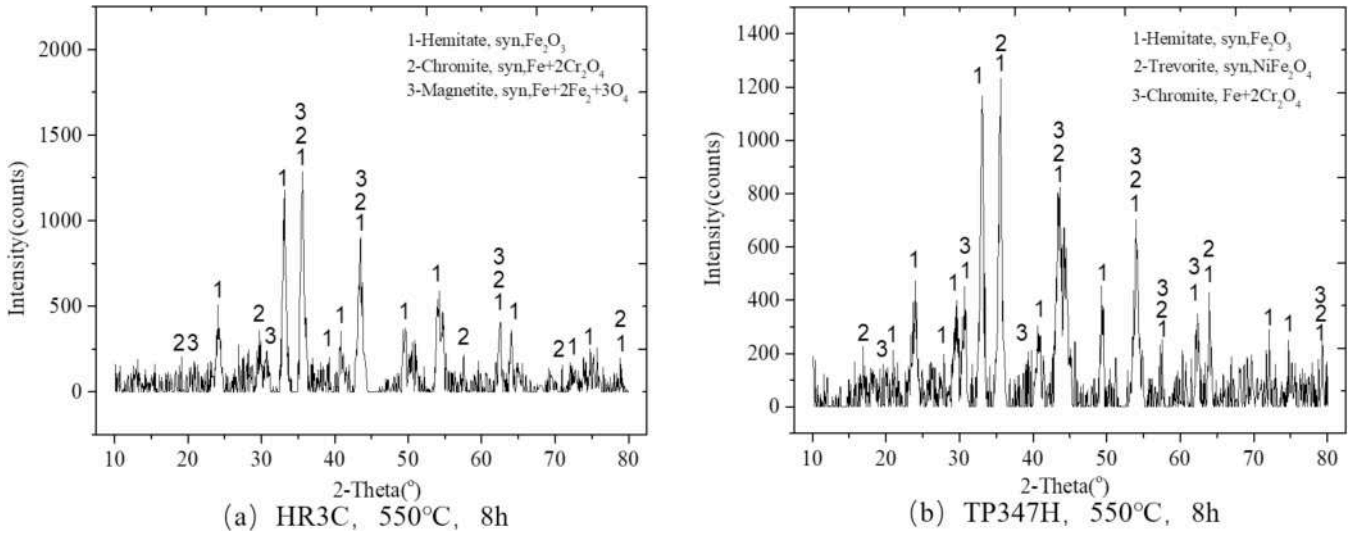

Fig. 15. XRD patterns of the corrosion layer at 550 °C ($2\%O_2+0.2\%SO_2+CO_2$) .

transition of S element to the salt particle and bulk.

3.3.4. $2\%O_2+0.3\%SO_2+20\%H_2O+CO_2$, 550 °C

It could be seen from Fig. 16 (a) that the HR3C corrosion layer consists mainly of Fe, Cr, and O elements, and that the K, S and O contents are enriched in the deposited salt layer, indicating that KCl causes prominent sulfation. The corrosion surface and sedimentary salt layer contain a high content of S and O suggesting a high sulfate level on the outside of the corrosion sheet. The corrosion layer is firmly attached to the matrix and is intact and dense, while the S element penetration-erosion behavior is also found in the bulk. The XRD analysis of the HR3C corrosion layer in Fig. 17 (a) shows that the main components are Fe_2O_3 and K_2SO_4. As shown in Fig. 16 (b), the outer edge of the corrosion layer is mainly composed of Fe, K and S elements. While at the interface between the corrosion layer and the substrate, the content of Cr and O elements are high. The corrosion layer is tightly bonded to the matrix, and it exhibits the phenomenon of the penetration of the S element into the matrix. The XRD analysis of the TP347H corrosion layer in Fig. 17 (b) shows that the main components are Fe_2O_3 and K_2SO_4, in addition, a kind of $MnSO_4$ is also found, which further indicating that the sulfate has a strong molten salt corrosion effect on TP347H.

In summary, compared with the results of corrosion weight gain at varied SO_2 concentrations, it can be seen that the phenomenon of KCl sulfation with 0.3% SO_2 is more significant than that with 0.2% SO_2. In the corrosion layer of both alloy materials, a high sulfate layer was formed, indicating that the formation of sulfates can aggravate the extent of molten salt corrosion.

3.4. Different corrosion reduction methods

3.4.1. Corrosion resistance coatings

There are three familiar coating methods used for the reduction of hazardous corrosion, (1) thermal spray, (2) metal infiltration, and (3) laser cladding. In the thermal spray process, the spray sources are heated to their melting or semi-melting point so that they can be sprayed on the substrate surface. Ni based coating is often used against high temperature corrosion due to its best corrosion resistance property and low porosity coating at high temperature environment (Oksa et al., 2013). Metal infiltration is subjected to high temperature diffusion and permeation process, reacts with the surface of the metal alloy, and forms alloying resistance to high temperature corrosion on the surface of the metal alloy. Kiamehr et al. (2017) conducts corrosion tests on FeAl, Fe_2Al, and Ni_2Al_3 coatings to analyze the best corrosion resistance coating. They found that Ni_2Al_3 coating did not experience severe corrosion after the exposure to high temperature and high KCl salt deposition. Laser cladding simultaneously melt the coating material and a thin layer of the substrate surface, and rapidly solidify to form a surface coating that is metallurgically bonded to the substrate. Laser cladding provides good corrosion and oxidation resistance of the coating, which is dense and uniform. In addition, the newly developed high-entropy alloy coatings with attractive and unique properties are also a potential choice for the future coating development.

In conclusion the coatings formed by thermal spray technology, metal infiltration, and laser cladding provide protection, increase the efficiency and life of the boiler. However, many problems still need to be faced e.g., coating is prone to cracking and flaking.

3.4.2. Biomass co-firing with other fuels

One of the major drawback of biomass combustion is the formation of severe fouling and harsh corrosion due to the high contents of alkali salts. To mitigate this severe effect, a short term solution is to co-fired biomass with other fuels having low corrosion risks (Wang et al., 2011). In this regard, a remarkably progress in biomass co-firing has been reported in the past decades (Yin, 2013). Montgomery et al. (2008) showed that co-firing biomass with other solid fuel like coal can significantly reduce the corrosion by converting the high corrosive alkali salt into less harmful alkali sulfate. Hence it is necessary to optimize the biomass co-firing blending ratio with other fuels. In general, the majority of co-firing biomass power plants use the ratio $\leq$40% to avoid the risks induced by co-firing (Montgomery et al., 2008).

In addition, co-firing biomass with sewage sludge was also reported previously, due to its rich contents of aluminium and iron sulphte, which is able to capture the KCl and convert it into low corrosive deposits (Aho et al., 2010).

3.4.3. In-situ corrosion prevention

One way to reduce the corrosion is to built the in-situ monitoring and regulating system. The results from our experiment and other research works illustrated that the temperature is very sensitive to the alloy corrosion. So in-situ regulating system for combustion process is used to control the temperature of boiler heater tubes. In combination with in-situ method the KCl concentration is measured in the flue gas and then spray some sulfate solution which is a selective way to prevent the corrosion. An ammonium sulfate solution specially prepared by Henderson et al. (2006) for the reduction of corrosion is sprayed into the flue gas. As a result KCl is effectively converted into K_2SO_4 which is much less corrosive than the KCl. Many other materials like aluminium, iron sulfate, and $Al_2O_3.SiO_2$ are also available for spraying into the furnace to effectively prevent the Cl from being deposited on the furnaces tube surfaces (Aho et al., 2010).

4. Conclusions

In this paper, the hot corrosion behaviors of two representative materials (TP347H, HR3C) used for superheaters in furnaces are studied. The effects of oxy-combustion atmosphere, KCl deposition, and temperature on the corrosion at the starting stage are investigated. The main conclusions are as follows:

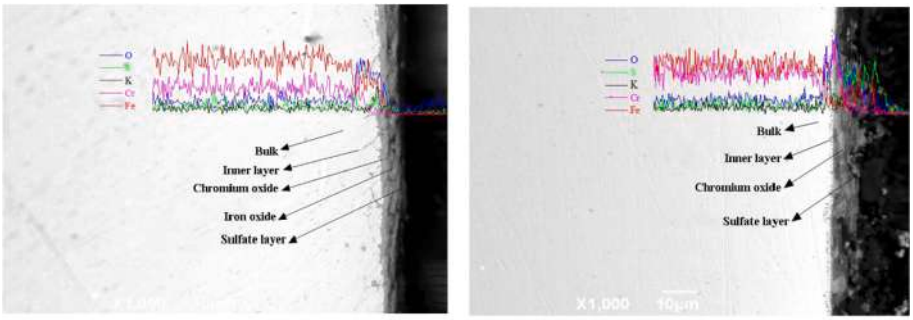

(a) HR3C, 550°C, 8h (b) TP347H, 550°C, 8h

Fig. 16. SEM and EDS line analysis of the sample cross-sections of HR3C and TP347H after 8 h ($2\%O_2+0.3\%SO_2+20\%H_2O+CO_2$) .

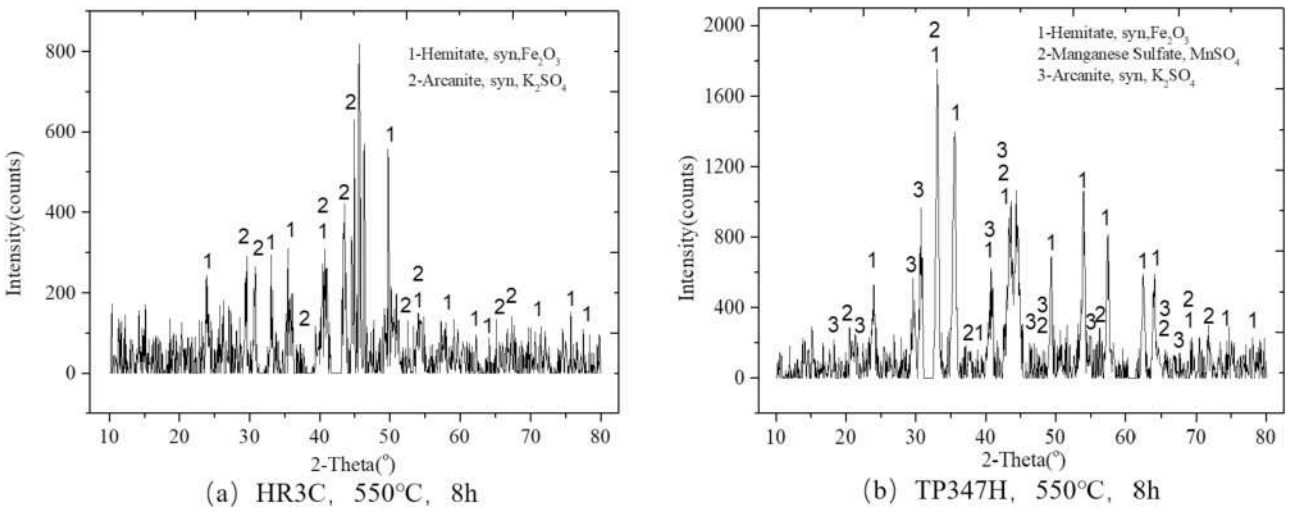

Fig. 17. XRD patterns of the corrosion layer at 550 °C ($2\%O_2+0.3\%SO_2+20\%H_2O + CO_2$) .

(1) The hot corrosion rate is significantly sped up by KCl deposition, more than five times the gas corrosion rate under the same gas composition and temperature. HR3C with higher Cr and Ni contents is more likely to form Cr enrichment on the interface between the corrosion layer and the substrate than TP347H, resulting in stronger resistance to the hot corrosion than TP347H.
(2) When the corrosion atmosphere is changed from air-combustion to oxy-combustion, the hot corrosion rate is reduced with a denser Cr oxide film and less metal sulfides. The increase of temperature in the presence of KCl deposition significantly affects the hot corrosion rate, e.g. the corrosion rate at 650 °C is 16 times higher than that at 450 °C.
(3) Water vapor and SO_2 are interacted, and have opposite influences on the hot corrosion. Compared to the dry environment, a high-humidity environment decreases the hot corrosion rate, by form denser and more protective oxide scale, while it could also tranfer the S element to alkali metal and oxide scale, which are two competitive factor to the corrosion process; however, a higher SO_2 concentration facilitates the sulfation of KCl deposits, leading to stronger damage to the chromium oxide film and thereby an increased hot corrosion rate.

Declaration of competing interests

The authors declare that they have no known competing financial interests or personal relationships that could have appeared to influence the work reported in this paper.

CRediT authorship contribution statement

Jiaye Zhang: Writing - original draft, Methodology. **Zia ur Rahman:** Writing - original draft, Methodology. **Xuebin Wang:** Investigation, Methodology. **Zhao Wang:** Investigation. **Peng Li:** Investigation. **Yongbing Wang:** Investigation. **Delige Bate:** Investigation. **Ke Zhao:** Writing - review & editing. **Houzhang Tan:** Methodology, Writing - review & editing.

Acknowledgments

The authors gratefully acknowledge the financial support of the National Natural Science Foundation of China (Nos. 51676157 and 51761125012), the Natural Science Foundation of Xinjiang Province (Nos. 2017D01B41 and 2017D01A69), the Fundamental Research Funds for the Central Universities, and Natural Science Basic Research Plan in Shaanxi Province of China (2017JZ010).

References

Aho, M., Yrjas, P., Taipale, R., Hupa, M., Silvennoinen, J., 2010. Reduction of superheater corrosion by co-firing risky biomass with sewage sludge. Fuel 89, 2376–2386.
Ani, M.H.B., Kodama, T., Ueda, M., Kawamura, K., Maruyama, T., 2009. The effect of water vapor on high temperature oxidation of Fe-Cr alloys at 1073 K. Mater. Trans. 50, 2656–2663.
Asteman, H., Svensson, J.-E., Johansson, L.-G., 2002. Oxidation of 310 steel in H_2O/O_2 mixtures at 600 °C: the effect of water-vapour-enhanced chromium evaporation. Corrosion Sci. 44, 2635–2649.
Blomberg, T., Tripathi, T., Karppinen, M., 2019. New chemical mechanism explaining the breakdown of protective oxides on high temperature steels in biomass combustion and gasification plants. RSC Adv. 9, 10034–10048.
Bordenet, B., 2008. Influence of novel cycle concepts on the high-temperature corrosion of power plants. Mater. Corros. 59, 361–366.
Cao, W., Li, J., Lue, L., Zhang, X., 2016. Release of alkali metals during biomass thermal conversion. Archives of Industrial Biotechnology 1, 1–3.
Chen, C., Luo, Z., Yu, C., Wang, T., Zhang, H., 2017. Transformation behavior of potassium during pyrolysis of biomass. RSC Adv. 7, 31319–31326.
Chen, L., Yong, S.Z., Ghoniem, A.F., 2012. Oxy-fuel combustion of pulverized coal: characterization, fundamentals, stabilization and CFD modeling. Prog. Energy Combust. Sci. 38, 156–214.
Ekvall, T., Andersson, K., Leffler, T., Berg, M., 2017. K–Cl–S chemistry in air and oxy-combustion atmospheres. Proc. Combust. Inst. 36, 4011–4018.
Grabke, H., Reese, E., Spiegel, M., 1995. The effects of chlorides, hydrogen chloride, and sulfur dioxide in the oxidation of steels below deposits. Corrosion Sci. 37, 1023–1043.
Henderson, P., Szakalos, P., Pettersson, R., Andersson, C., Högberg, J., 2006. Reducing superheater corrosion in wood-fired boilers. Mater. Corros. 57, 128–134.
Henriksson, M., Warnqvist, B., 1979. Kinetics of formation of HCl (g) by the reaction between NaCl (s) and SO_2, O_2, and H_2O (g). Ind. Eng. Chem. Process Des. Dev. 18, 249–254.
Holcomb, G.R., Tylczak, J., Meier, G.H., Jung, K.Y., Mu, N., Yanar, N., Pettit, F., 2012. Fireside corrosion in oxy-fuel combustion of coal. ECS Transactions 41, 73–84.
Holcomb, G.R., Tylczak, J., Meier, G.H., Lutz, B.S., Jung, K., Mu, N., Yanar, N.M., Pettit, F.S., Zhu, J., Wise, A., 2013. Fireside corrosion in oxy-fuel combustion of coal. Oxid. Metals 80, 599–610.
Hu, Z., Wang, X., Adeosun, A., Ruan, R., Tan, H., 2018. Aggravated fine particulate matter emissions from heating-upgraded biomass and biochar combustion: the effect of pretreatment temperature. Fuel Process. Technol. 171, 1–9.
Karlsson, S., Jonsson, T.r., Hall, J., Svensson, J.-E., Liske, J., 2014. Mitigation of fireside corrosion of stainless steel in power plants: a laboratory study of the influences of SO_2 and KCl on initial stages of corrosion. Energy & fuels 28, 3102–3109.
Kiamehr, S., Lomholt, T.N., Dahl, K.V., Christiansen, T.L., Somers, M.A., 2017. Application of aluminum diffusion coatings to mitigate the KCl-induced high-temperature corrosion. Mater. Corros. 68, 82–94.
Lehmusto, J., Yrjas, P., Skrifvars, B.-J., Hupa, M., 2012. High temperature corrosion of superheater steels by KCl and K_2CO_3 under dry and wet conditions. Fuel Process. Technol. 104, 253–264.
Lin, Z.J., Li, M.S., Wang, J.Y., Zhou, Y.C., 2007. High-temperature oxidation and hot corrosion of Cr_2AlC. Acta Mater. 55, 6182–6191.
Little, J.A., 2008. Mater. Char. 59, 104.
Mahajan, S., Chhibber, R., 2019. Hot corrosion studies of boiler steels exposed to different molten salt mixtures at 950 °C. Eng. Fail. Anal. 99, 210–224.
Mahobia, G., Paulose, N., Singh, V., 2013. Hot corrosion behavior of superalloy IN718 at 550 and 650 °C. J. Mater. Eng. Perform. 22, 2418–2435.

McKee, D., Shores, D., Luthra, K., 1978. The effect of SO_2 and NaCl on high temperature hot corrosion. J. Electrochem. Soc. 125, 411–419.
Meißner, T., Montero, X., Fähsing, D., Galetz, M., 2019. Cr diffusion coatings on a ferritic-martensitic steel for corrosion protection in KCl-rich biomass co-firing environments. Corrosion Sci. 108343.
Mlonka-Mędrala, A., Magdziarz, A., Kalemba-Rec, I., Nowak, W., 2019. The influence of potassium-rich biomass ashes on steel corrosion above 550 °C. Energy Convers. Manag. 187, 15–28.
Montgomery, M., Vilhelmsen, T., Jensen, S., 2008. Potential high temperature corrosion problems due to co-firing of biomass and fossil fuels. Mater. Corros. 59, 783–793.
Okoro, S.C., Kiamehr, S., Montgomery, M., Frandsen, F.J., Pantleon, K., 2017. Effect of flue gas composition on deposit induced high temperature corrosion under laboratory conditions mimicking biomass firing. Part II: exposures in SO_2 containing atmospheres. Mater. Corros. 68, 515–528.
Okoro, S.C., Montgomery, M., Frandsen, F.J., Pantleon, K., 2015. Effect of water vapor on high-temperature corrosion under conditions mimicking biomass firing. Energy & Fuels 29, 5802–5815.
Oksa, M., Tuurna, S., Varis, T., 2013. Increased lifetime for biomass and waste to energy power plant boilers with HVOF coatings: high temperature corrosion testing under chlorine-containing molten salt. J. Therm. Spray Technol. 22, 783–796.
Otsuka, N., 2008. A thermodynamic approach on vapor-condensation of corrosive salts from flue gas on boiler tubes in waste incinerators. Corrosion Sci. 50, 1627–1636.
Paneru, M., Stein-Brzozowska, G., Maier, J.r., Scheffknecht, G.n., 2013. Corrosion mechanism of alloy 310 austenitic steel beneath NaCl deposit under varying SO_2 concentrations in an oxy-fuel combustion atmosphere. Energy & fuels 27, 5699–5705.
Paul, S., Harvey, M., 2013. Corrosion testing of Ni alloy HVOF coatings in high temperature environments for biomass applications. J. Therm. Spray Technol. 22, 316–327.
Pettersson, J., Folkeson, N., Johansson, L.-G., Svensson, J.-E., 2011. The effects of KCl, K_2SO_4 and K_2CO_3 on the high temperature corrosion of a 304-type austenitic stainless steel. Oxid. Metals 76, 93–109.
Pettersson, J., Svensson, J.E., Johansson, L.G., 2008. Alkali induced corrosion of 304-type austenitic stainless steel at 600 °C; comparison between KCl, K_2CO_3 and K_2SO_4, Materials science forum. Trans Tech Publ 367–375.
Sher, F., Pans, M.A., Sun, C., Snape, C., Liu, H., 2018. Oxy-fuel combustion study of biomass fuels in a 20 kWth fluidized bed combustor. Fuel 215, 778–786.
Smith, J.S., Safferman, S.I., Saffron, C., 2019. Development and application of a decision support tool for biomass co-firing in existing coal-fired power plants. J. Clean. Prod. 236, 117375–117388.
Wang, X., Tan, H., Niu, Y., Pourkashanian, M., Ma, L., Chen, E., Liu, Y., Liu, Z., Xu, T., 2011. Experimental investigation on biomass co-firing in a 300 MW pulverized coal-fired utility furnace in China. Proc. Combust. Inst. 33, 2725–2733.
Yin, C., 2013. Biomass Co-firing, Biomass Combustion Science, Technology and Engineering. Elsevier, pp. 84–105.
Yu, X., Song, P., He, X., Khan, A., Huang, T., Li, C., Li, Q., Lü, K., Chen, K., Lu, J., 2019. Influence of the combined-effect of NaCl and Na_2SO_4 on the hot corrosion behaviour of aluminide coating on Ni-based alloys. J. Alloys Compd. 790, 228–239.
Zeng, Z., Natesan, K., Cai, Z., Rink, D., 2014. Effect of coal ash on the performance of alloys in simulated oxy-fuel environments. Fuel 117, 133–145.